論文 / 著書情報
Article / Book Information

Title	Spatial distribution diagnosis of electron temperature and density of argon inductively coupled plasma by tomographic optical emission spectroscopic measurement and collisional-radiative model
Authors	Yuya Yamashita, Kenta Doi, Tetsuji Kiyota, Kenta Ishi, Shuhei Watanabe, Wataru Kikuchi, Atsushi Nezu, Hiroshi Akatsuka
Citation	Journal of Vacuum Science & Technology A, Vol. 42, No. 2, 023003
Pub. date	2024, 1
DOI	https://dx.doi.org/10.1116/6.0003209
note	This article may be downloaded for personal use only. Any other use requires prior permission of the author and the American Vacuum Society (AVS). This article appeared in Yuya Yamashita et al., J. Vac. Sci. Technol. A, 42, 023003,(2024) and may be found at https://doi.org/10.1116/6.0003209

JVST A
Journal of Vacuum Science & Technology A

ARTICLE

pubs.aip.org/avs/jva

Spatial distribution diagnosis of electron temperature and density of argon inductively coupled plasma by tomographic optical emission spectroscopic measurement and collisional-radiative model

Cite as: J. Vac. Sci. Technol. A **42**, 023003 (2024); doi: 10.1116/6.0003209
Submitted: 10 October 2023 · Accepted: 2 January 2024 ·
Published Online: 29 January 2024

Yuya Yamashita,[1,2,a)] Kenta Doi,[3] Tetsuji Kiyota,[4] Kenta Ishi,[1] Shuhei Watanabe,[1] Wataru Kikuchi,[1] Atsushi Nezu,[5,6] and Hiroshi Akatsuka[1,6]

AFFILIATIONS

[1]Department of Electrical and Electronic Engineering, School of Engineering, Tokyo Institute of Technology, 2-12-1-N1-10 Ookayama, Meguro-ku, Tokyo 152-8550, Japan
[2]Research Fellow DC, Japan Society for the Promotion of Science, Kojimachi Business Center Building, 5-3-1 Kojimachi, Chiyoda-ku, Tokyo 102-0083, Japan
[3]Institute of Advanced Technology, ULVAC, Inc., 1220-1 Suyama, Susono-shi, Shizuoka 410-1231, Japan
[4]Strategic Planning Department, ULVAC, Inc., 2500 Hagisono, Chigasaki-shi, Kanagawa 253-8543, Japan
[5]Safety and Radiation Management Division, Open Facility Center, Tokyo Institute of Technology, 2-12-1-N1-10 Ookayama, Meguro-ku, Tokyo 152-8550, Japan
[6]Laboratory for Zero-Carbon Energy, Institute of Innovative Research, Tokyo Institute of Technology, 2-12-1-N1-10 Ookayama, Meguro-ku, Tokyo 152-8550, Japan

[a)]**Author to whom correspondence should be addressed:** yamashita.y.an@m.titech.ac.jp

ABSTRACT

There are few reported cases in which the spatial distribution of spectral emission coefficients of plasmas from tomographic optical emission spectroscopy measurements is analyzed based on a collisional-radiative model to diagnose the spatial distribution electron temperature of T_e and density N_e. This study aimed at *in situ* diagnosis of process plasma. The spectral radiance of 18 lines-of-sight was measured simultaneously in argon inductively coupled plasma. The spatial distribution of the excited level number density distribution was calculated from the spatial distribution of spectral emission coefficients obtained from spectral tomography calculations. The three-dimensional distribution of T_e and N_e was analyzed using a collisional-radiative model from the obtained spatial distribution of the excited levels number density. The effects of power and pressure on the dependence of the spatial distribution of T_e and N_e were discussed. Furthermore, data processing methods for spectral tomographic measurements with coarse wavelength resolution were also discussed.

I. INTRODUCTION

In recent years, the field of plasma processing has seen progress in the size of workpieces, the miniaturization of processed structures, and high aspect ratios. As a result, there is a growing demand for diagnostics of the spatial distribution of plasma macroparameters. Indeed, there has been an increasing number of reports on the diagnosis of the spatial distribution of plasma by tomographic measurement. Optical emission spectroscopic (OES) measurement is a simple noncontact diagnostic method that can be realized using an experimental system and is suitable for

performing real-time measurements of processing plasmas. Diagnosis of the spatial distribution of plasma using tomography and emission spectroscopy, specifically in the field of fusion reactor plasmas,[1] has been considered for a long time. Inverse integral calculations, such as the Radon transform, have previously been utilized, and with improvements in computer performance, some studies have also used discrete tomography.[2]

In a prior study[3] on air plasma arc jet, simultaneous five-line-of-sight spectroscopy was performed by placing several mirrors inside the vessel and guiding the reflected light to a lens placed in front of the entrance slit of the spectrometer. The study diagnosed the excitation temperature distribution as well as the rotational and vibrational temperatures. In the prior study, a diffraction grating movable polychromator was used. This facilitates measurement over a wide wavelength range with high wavelength resolution. However, a fixed reflector and mirror are used as the incident optical system to the spectrometer, which limits the number of lines-of-sight. In addition, the complexity of the incident optics makes it difficult to apply this method to process plasmas at a reduced pressure.

In Barni *et al.*'s study[4] of toroidal field confined plasmas, 19 lines-of-sight were positioned. Each of the lines-of-sight was taken sequentially at different times. The excitation temperature of the hydrogen plasma was thus diagnosed. Tomographic measurements with a single line-of-sight spectrometer were achieved by taking multiple random line-of-sight measurements and averaging the results. However, the method did not acquire all the lines-of-sight simultaneously. In that method, the uncertainty of the reconstructed image may increase due to plasma time evolution.

An example of tomographic optical emission spectroscopy of an inductively coupled plasma[5,6] has been reported. As the result of spectral tomography, the spatial distribution of the excited-level number density distribution was obtained. In the prior study, a single fiber that had a position-variable lens head with a four-axis robot was employed as the input optical system to the monochromator. The system deserves special mention for its ability to change observation positions quickly and freely. However, the system was mechanically complicated.

In low-temperature weakly ionized process plasmas, diagnostics of electron temperature T_e and density N_e are important.[7] However, there are few reported cases of T_e and N_e by tomography measurements in weakly ionized plasmas. Moreover, most of them employ the line-pair method, which is extremely undesired for non-equilibrium ionized plasmas.

Tomographic OES measurements were performed on arc plasmas by arranging a photometric system with a plasma source on the rotation stage and a movable one-line-of-sight lens.[8] The temperature, ionization coefficient, electron (ion) density, and atomic density were obtained using the line-pair method.

Rathore *et al.*[9] entailed tomographic OES measurements on microwave-induced plasma using eight pinhole cameras with wavelength filters. The spatial distributions of the T_e and N_e were obtained by assuming a coronal equilibrium.

Gonzalez-Fernandez *et al.* performed tomographic optical emission spectroscopy in a linearly magnetized plasma system with 49 lensed fibers.[10] T_e and N_e were obtained using the line-pair method with the assumption of corona model.

However, these reports assume simplified excitation kinetics. Introducing that assumption has the advantage of facilitating a rough understanding of atomic-molecular processes and contributes to reducing the computational complexity of excitation kinetic calculations. On the other hand, it limits the applicable plasma macroparameters; therefore, there are limits to the types of plasma (for ionized plasma or recombination plasma) where the applied excitation kinetics is validated.[11]

The collisional-radiative (CR) model is a type of excitation kinetic model that takes macroparameters such as the temperature (of electrons, atoms, and ions), density (of electrons, atoms, and ions), and pressure as inputs, calculates the rates of various elementary processes, and outputs an excited-level number density distribution by analyzing the rate equations. In principle, the CR model can be applied to a wide range of macroparameters, making it a highly versatile excitation kinetic model. Experimental data from tomographic OES measurements must be analyzed by a CR model that can faithfully describe atomic and molecular processes. However, only one study using such a strategy has been reported,[12] where in tomographic optical emission spectroscopy was performed in the plume region of a Hall-thruster Ar plasma using radon conversion. In the study, the Hall-thruster on a rotating and $x-y$ (horizontal) stages was installed in a vacuum chamber (diameter: 1.5 m, length: 3.0 m). A fiber with a lens on the z (vertical) stage was also installed in the vacuum chamber. Spectra were took for every 10° rotations of the stage. The imaging was repeated at 69 points by scanning the x stage; in total, 1242(=69 × 10) line-of-sight of measurements sequentially. Through spectral tomographic analysis and CR modeling, the x-y distributions of T_e and N_e were diagnosed. It was noted that the time difference between acquiring the spectra could be a source of increased uncertainty in the reconstruction.

In the field of semiconductor processing, various plasmas with different temperatures, pressures, and principles are in general use.[13] However, spatial *in situ* diagnoses applicable to these plasmas have not been realized.[14] With the above background, plasma diagnostics based on the combination of spectroscopic tomography measurements and CR modeling should be applied to semiconductor process plasmas.

Our study aims to diagnose the spatial distribution of T_e and N_e in plasmas by analyzing the spatial distribution of the spectral emission coefficients of plasmas obtained using tomographic emission spectroscopy measurements, based on a CR model. An argon low-pressure discharge plasma generated by an inductively coupled plasma system is used as the experimental target. The basic characteristics of plasma are observed. The findings will serve as a basis for future plasma experiments on other gas species. The present study aims to realize diagnosis that has a more noninvasive experimental system and a more versatile atomic and molecular process analysis.

The feature of the experimental system is that a radiometric system was constructed to simultaneously acquire spectra of 18 lines-of-sight, including intersecting lines-of-sight. Uncertainties of reconstructed image due to time fluctuations will prevent by acquiring all line-of-sight lines at the same time. Spectral radiance is observed by lenses placed outside the chamber through the windows. This eliminates the need to place the optical system in a vacuum and reduces the observation window area of the device, making it more applicable to actual process equipment.

The first feature of the analysis is that the CR model was employed for the atomic and molecular process model to achieve an analysis. This enables the analysis with the possibility of hand extension to plasma diagnostics with different generation principles. The second feature of the analysis is that the constrained regularization algorithm, a type of (pixel-based) reconstruction, is extended as a wavelength function for spectral. Furthermore, we will propose a method of wavelength interpolation and extraction of emission lines for processing experimental data in spectral tomography measurements using a multichannel spectrometer.

II. EXPERIMENTS

A. Optical emission spectroscopic measurement of plasma

Figure 1 shows the experimental inductively coupled plasma (ICP)-generating apparatus employed in this study. The inner wall of the chamber was anodized aluminum (pressurized steam sealing, VACAL-SAL2V3010A, ULVAC TECHNO, Ltd.). A spiral-shaped radio frequency (RF) antenna was placed at the top of the chamber over the top window (synthetic quartz, diameter: 205 mm, thickness: 21.5 mm). The side-view window (synthetic quartz, height 115 mm × width 10 mm, thickness 6 mm) was placed on the chamber sidewall. Argon (Ar) gas was supplied to the chamber via a mass flow controller. The chamber was evacuated using turbomolecular and rotary pumps. The base pressure of the vacuum chamber was 1.5×10^{-5} Pa. A 13.56 MHz RF power was applied to the RF antenna to generate the plasma.

Eight and ten collimator lenses (#88-173, Edmond Optics) were placed on the outside window of the side ($+y$ side) and top ($+z$ side) of the chamber, respectively, as shown in Fig. 2. The collimator lenses were connected to a multichannel spectrometer (M116, Horiba, focal length: 116 mm) with optical fibers (core diameter: 100 μm). The line-of-sight dependence of spiral radiance at the air-side surface on the window $L_{\text{plasma air}}(\lambda)$ was measured by the multichannel spectrometer as described in Sec. II B.

B. Spectral radiance calibration and Fresnel reflection correction

The spectral radiometry system was calibrated using a setup as shown in Fig. 3. A spectral radiance surface[15] was realized using a spectral irradiance standard lamp (JPD100V500WCS, Ushio Lighting) and a standard diffuse reflector (SG 3051, SphereOptics). The spectral irradiance standard lamp was driven at a constant voltage of DC 95.0V (the specified voltage as the standard lamp) by a DC power supply unit (PSW-720M160, TEXIO TECHNOLOGY CORPORATION). The voltage was measured using the four-terminal method to prevent measurement errors due to voltage drop in electric wires. The light shields with hole[15] were placed between the spectral irradiance standard lamp and the standard diffuse reflector. The hole size of the light shields is larger than the line connecting the outline of the bulb of the spectral irradiance standard lamp and the outline of the standard diffuse reflector. Therefore, direct light is not blocked, while stray light is blocked.

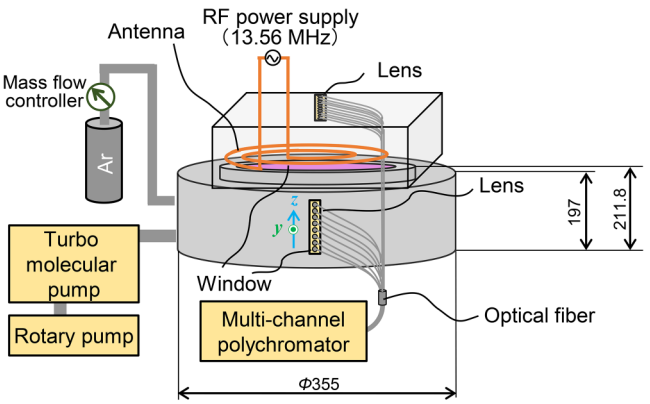

FIG. 1. Schematic of ICP-generating apparatus. The sizes are denoted at the chamber internal.

The spectral radiance on the standard diffuse reflector surface $L_{\text{std}}(\lambda)$ was obtained as shown in Fig. 4 and as follows:

$$L_{\text{std}}(\lambda) = \frac{R_{\text{std}}(\lambda)}{\pi} E_{\text{std}}(\lambda), \tag{1}$$

where $R_{\text{std}}(\lambda)$ is the calibration value of the spectral total reflectance of the standard diffuse reflector and $E_{\text{std}}(\lambda)$ is the calibration value of the spectral irradiance standard lamp at 500 mm in front. It must be noted that $R_{\text{std}}(\lambda)$ and $E_{\text{std}}(\lambda)$ were discretely calibrated at 1 and 5 nm intervals, respectively. The interpolated values $S_{\text{lagr}}(\lambda)$

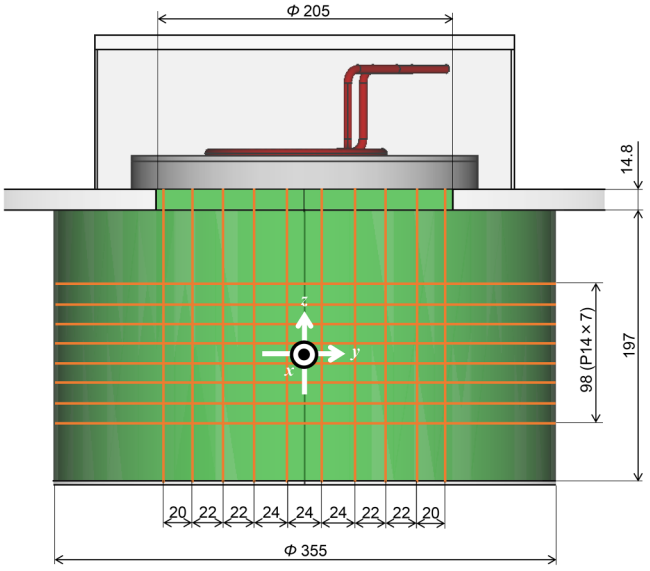

FIG. 2. Lines-of-sight of the spectral radiance measurements on the chamber windows.

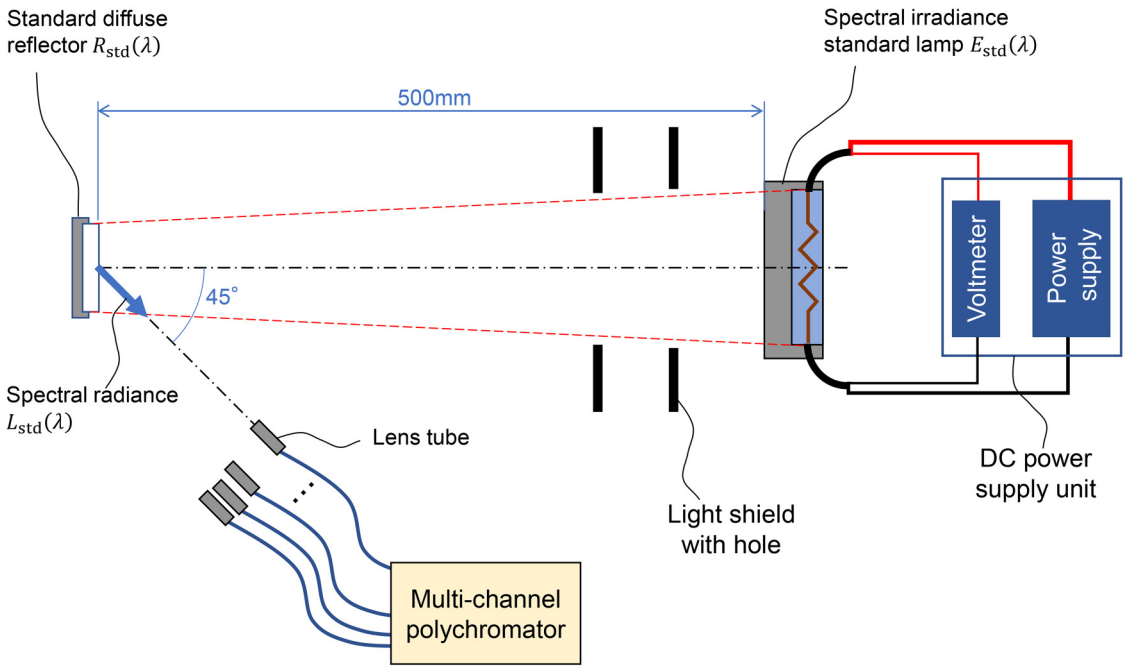

FIG. 3. Experiment setup of spectrometer spectral radiance calibration.

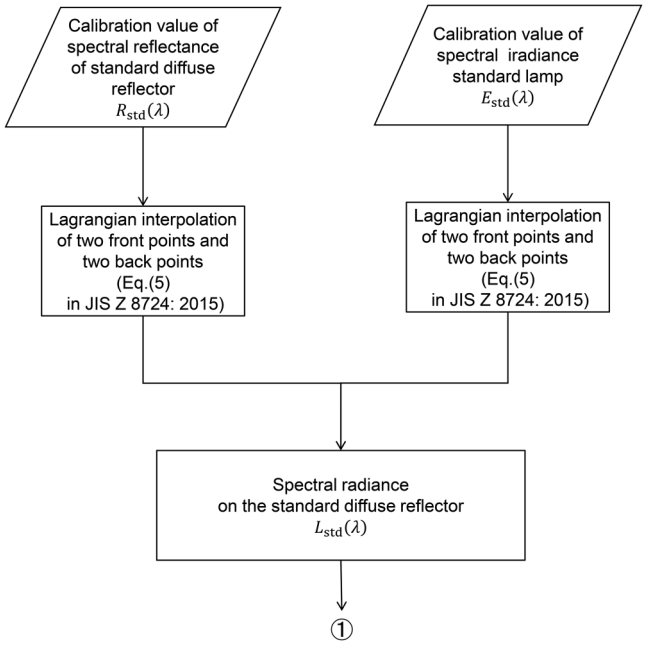

FIG. 4. Calculation flowchart of the spectral radiance on the standard diffuse reflector $L_{std}(\lambda)$.

at any wavelength λ in the middle were calculated using the Lagrangian interpolation of the calibrated values of two front points: $S_1(\lambda_1)$ and $S_2(\lambda_2)$, and two back points $S_3(\lambda_3)$ and $S_4(\lambda_4)$, which is shown in Eq. (5) of JIS Z 8724:2015[16] as follows:

$$S_{lagr}(\lambda) = \frac{(\lambda-\lambda_2)(\lambda-\lambda_3)(\lambda-\lambda_4)}{(\lambda_1-\lambda_2)(\lambda_1-\lambda_3)(\lambda_1-\lambda_4)}S_s(\lambda_1) + \frac{(\lambda-\lambda_1)(\lambda-\lambda_3)(\lambda-\lambda_4)}{(\lambda_2-\lambda_1)(\lambda_2-\lambda_3)(\lambda_2-\lambda_4)}S_s(\lambda_2) + \frac{(\lambda-\lambda_1)(\lambda-\lambda_2)(\lambda-\lambda_4)}{(\lambda_3-\lambda_1)(\lambda_3-\lambda_2)(\lambda_3-\lambda_4)}S_s(\lambda_3) + \frac{(\lambda-\lambda_1)(\lambda-\lambda_2)(\lambda-\lambda_3)}{(\lambda_4-\lambda_1)(\lambda_4-\lambda_2)(\lambda_4-\lambda_3)}S_s(\lambda_4), \quad (2)$$

where $\lambda_1 < \lambda_2 < \lambda < \lambda_3 < \lambda_4$.

The count value when observing the spectral radiance standard plane: $I_{std\ gross}(\lambda)$ was measured by the experimental setup as shown in Fig. 3 for each channel (per fiber with lens). Furthermore, the dark count value: $I_{std\ dark}(\lambda)$ was measured by the same system in turning off the spectral irradiance standard lamp.

Therefore, the net value of the spectral radiance of the plasma at the air-side of the window surface: $L_{plsma\ air}(\lambda)$ was calculated for each channel as shown in Fig. 5 and as expressed in the following

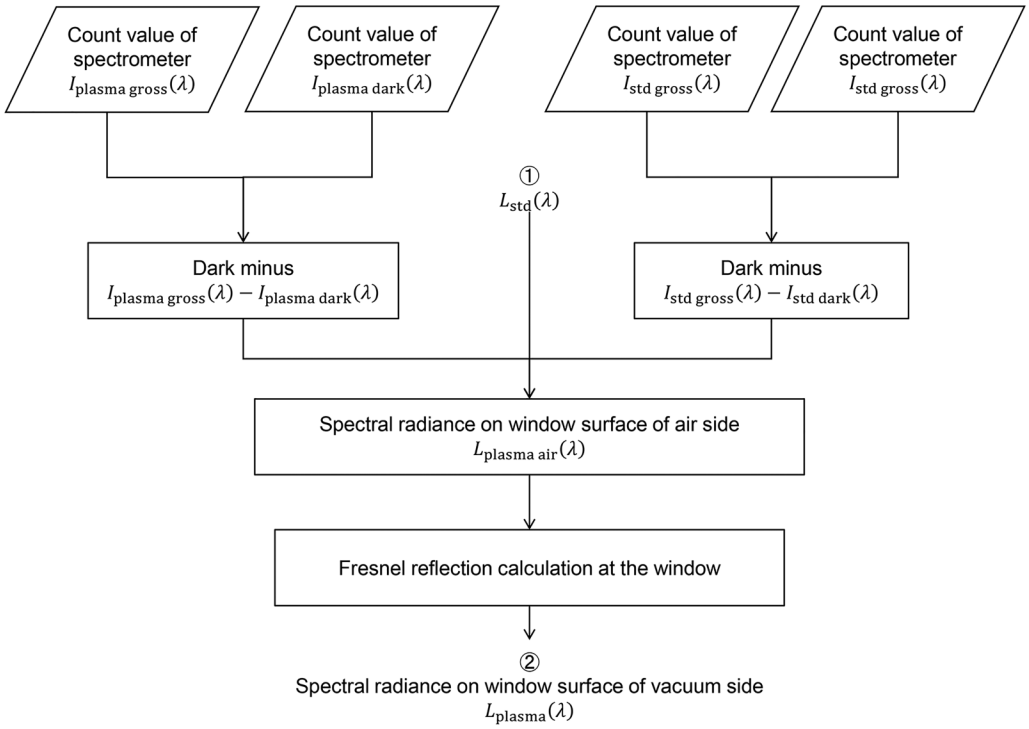

FIG. 5. Calculation flowchart of the spectral radiance of plasma.

equation:

$$L_{\text{plsma air}}(\lambda) = L_{\text{std}}(\lambda)\frac{I_{\text{plasma gross}}(\lambda) - I_{\text{plasma dark}}(\lambda)}{I_{\text{std gross}}(\lambda) - I_{\text{std dark}}(\lambda)}, \quad (3)$$

where $I_{\text{plasma gross}}(\lambda)$ and $I_{\text{plasma dark}}(\lambda)$ are the count values during the plasma discharge and when the plasma was switched off, respectively; the numerator and denominator denote the net count values of plasma and spectral radiance standard surface measurements, respectively.

Fresnel reflections occur at the window-air and window-vacuum interfaces. Therefore, the spectral radiance at the vacuum-side surface of the window $L_{\text{plasma}}(\lambda)$ was calculated from $L_{\text{plasma air}}(\lambda)$ using the correction formula[17] of the function of the window thickness and the refractive index of the window as shown in Fig. 5.

III. SPECTROSCOPIC TOMOGRAPHY CALCULATION

This section outlines the principles of spectral tomography calculations using the constrained regularization algorithm and then describes the data processing scheme of the spectral tomography calculation implemented in this study.

A. Constrained regularization algorithm

The constrained regularization algorithm[2,18] is a type of algorithm for algebraic (pixel-based) reconstruction in tomographic calculations. In this study, we developed a spectral tomography program by extending to wavelength function based on Ferreira *et al.*'s constrained regularization source code.[19,20]

$L_i(\lambda)$ is the measured projection [in this study, it corresponds to $L_{\text{plasma}}(\lambda)$] of the ith lens ($i = 1, 2, \ldots, n_{\text{v}} + n_{\text{h}}$, where $n_{\text{v}} = 8$ and $n_{\text{h}} = 10$ are the number of line-of-sight of vertical and horizontal directions, respectively.). n_{cols}(for column) $\times$ n_{rows}(for row) pixels reconstruction plane is considered, which were assumed 57×39 in this study. Note that the actual dimensions per pixel of the reconstructed image plane for y and z directions: Δy and Δz are derived from the above definition as follows, respectively:

$$\Delta y = \frac{y_{\max} - y_{\min}}{n_{\text{cols}}}, \quad (4)$$

$$\Delta z = \frac{z_{\max} - z_{\min}}{n_{\text{rows}}}, \quad (5)$$

where $y_{\max}$ and $y_{\min}$ are the y coordinates of the maximum and minimum values in the pixel plane, respectively; $z_{\max}$ and $z_{\min}$ are the z coordinates of the maximum and minimum values in the pixel plane, respectively. In this study, $y_{\max}$, $y_{\min}$, $z_{\max}$, and $z_{\min}$ were assumed $+19.0$, -19.0, $+13.0$, and -13.0 cm, receptively. Therefore, Δy and Δz were also 0.6667 cm/pixel.

$\varepsilon_j(\lambda)$ is the reconstructed image (corresponding to the spectral emission coefficient) of the jth pixel ($j = 1, 2, \ldots, n_{\text{rows}} \times n_{\text{cols}}$)

$$\begin{bmatrix} L_1(\lambda) \\ L_2(\lambda) \\ \vdots \\ L_{n_v+n_h}(\lambda) \end{bmatrix} = \begin{bmatrix} P_{1,1} & P_{1,2} & \cdots & P_{1,(n_{col}\times n_{row})} \\ P_{2,1} & P_{2,2} & \cdots & P_{2,(n_{col}\times n_{row})} \\ \vdots & \vdots & \ddots & \vdots \\ P_{(n_v+n_h),1} & P_{(n_v+n_h),2} & \cdots & P_{(n_v+n_h),(n_{col}\times n_{row})} \end{bmatrix} \times \begin{bmatrix} \varepsilon_1(\lambda) \\ \varepsilon_2(\lambda) \\ \vdots \\ \varepsilon_{(n_{col}\times n_{row})}(\lambda) \end{bmatrix}, \quad (6)$$

where $P_{i,j}$ is the projection (in this study, $P_{i,j}$ corresponds to the length of the ith line-of-sight on the jth pixel). We designated the projection vector, projection matrix, and image vector as $\mathbf{L}$, $\mathbf{P}$, and $\boldsymbol{\varepsilon}$, respectively. Equation (6) can be written as follows:

$$\mathbf{L} = \mathbf{P}\boldsymbol{\varepsilon}. \quad (7)$$

In an ideal situation, where the image is completely reconstructed, the left and right sides of Eqs. (6) and (7) are equal. However, the left and right sides did not match perfectly owing to numerical calculation errors. To find $\boldsymbol{\varepsilon}$ from $\mathbf{L}$, we must find the inverse of $\mathbf{P}$; however, because $\mathbf{P}$ is irregular, we cannot define the inverse of $\mathbf{P}$. Therefore, $\boldsymbol{\varepsilon}$ cannot be obtained analytically. Thus, the main objective of this reconstruction algorithm is to numerically find $\boldsymbol{\varepsilon}$, which minimizes the residual difference ϕ between $\mathbf{L}$ and $\mathbf{P}\boldsymbol{\varepsilon}$,

$$\phi = \|\mathbf{L} - \mathbf{P}\boldsymbol{\varepsilon}\|^2 + \boldsymbol{\alpha_1}\|\mathbf{D}_h\boldsymbol{\varepsilon}\|^2 + \boldsymbol{\alpha_2}\|\mathbf{D}_v\boldsymbol{\varepsilon}\|^2 + \boldsymbol{\alpha_3}\|\mathbf{I}_o\boldsymbol{\varepsilon}\|^2, \quad (8)$$

where $\alpha_1 (>0)$ is the regularization parameter that determines the calculation errors of $\mathbf{L}$ and $\mathbf{P}\boldsymbol{\varepsilon}$, α_1 was given as 1×10^{-5}; α_2 and α_3 are defined as follows:

$$\alpha_2 = \alpha_1, \quad (9)$$

$$\alpha_3 = 10\alpha_2. \quad (10)$$

$\mathbf{D}_h$, $\mathbf{D}_v$, and $\mathbf{I}_o$ are regularization matrices,

$$\mathbf{D}_h = \mathbf{E} - \mathbf{A}, \quad (11)$$

where $\mathbf{E}$ is an $n_{rows}n_{cols}$-dimensional identity matrix and $\mathbf{A} = [a_{i,j}]$ as follows:

$$a_{i,j} = \begin{cases} 1 & [j = i+1 \text{ (for } i = 1, 2, \ldots, (n_{rows}n_{cols} - 1))] \\ 1 & (i = n_{rows}n_{cols},\ j = 1) \\ 0 & \text{(else)}, \end{cases} \quad (12)$$

$$\mathbf{D}_v = \mathbf{E} - \mathbf{B}, \quad (13)$$

where $\mathbf{B} = [b_{i,j}]$ as follows:

$$b_{i,j} = \begin{cases} 1 & [j = i + n_{cols}\,(\text{for } i = 1, 2, \ldots, (n_{rows}n_{cols} - n_{cols}))] \\ 1 & [j = 1, 2, \ldots, n_{cols},\,(\text{for } i = (n_{rows}n_{cols} - n_{cols} + 1), \ldots, n_{rows}n_{cols})] \\ 0 & \text{(else)} \end{cases} \quad (14)$$

and $\mathbf{I}_o$ is a mask matrix, and the elements inside the ellipse [half axes are (n_{rows}, n_{cols}) and whose center is $(0, 0)$] are 0, and the other elements are 1.

Here, the pseudoinverse matrix M of P is defined as

$$\boldsymbol{\varepsilon} = \mathbf{M}\cdot\mathbf{L}. \quad (15)$$

From the above discussion, M can be expressed as

$$\mathbf{M} = \left(\mathbf{P}^T\mathbf{P} + \alpha_1\mathbf{D}_h^T\mathbf{D}_h + \alpha_2\mathbf{D}_v^T\mathbf{D}_v + \alpha_3\mathbf{I}_o^T\mathbf{I}_o\right)^{-1}\mathbf{P}^T. \quad (16)$$

Therefore, the reconstructed image $\boldsymbol{\varepsilon}$, which corresponds to the dependence of the spectral emission coefficient on the position $\varepsilon_j(\lambda)$, can be obtained.

B. Spectral tomography calculation

This section describes the data processing algorithm to spectral tomography on tomography calculation. The algorithm was developed in this study. Figure 6 shows the flow of data processing for spectral tomography calculation. Generally, in multichannel spectrometers, even if the pixels belong to the same row in the pixel plane of the image-receiving surface, the corresponding wavelengths are different for each row. However, to perform spectral tomography calculations, the dependence of spectral emissions between channels on the same wavelength has to be obtained. Therefore, in this study, linear interpolation of one front point and one back point was used to obtain the spectral radiance at any wavelength from the experimental spectral radiance data. The linear interpolated value $S_{linear}(\lambda)$ at λ was obtained with the experimental data points of the front $S_1(\lambda_1)$ and the back $S_2(\lambda_2)$ as follows:

$$S_{linear}(\lambda) = \frac{\lambda - \lambda_2}{\lambda_1 - \lambda_2}S_1(\lambda_1) + \frac{\lambda - \lambda_1}{\lambda_2 - \lambda_1}S_2(\lambda_2), \quad (17)$$

where $\lambda_1 < \lambda < \lambda_2$. The reasons for adopting this interpolation method are as follows: The mean slit wavelength width (wavelength resolution, determined by pixel width) of the spectrometer employed in this study is 2.19 nm. The mean measurement wavelength interval (determined by pixel interval) of the spectrometer employed in this study is 0.38 nm. Since the natural width of the argon spectrum is sufficiently narrow, linear interpolation at one point, before and after, was performed. In this study, the $L_{plasma}(\lambda)$ of each channel (CH) was interpolated by 0.2 nm at wavelengths of 350.0–972.8 nm. These were substituted into Eq. (15), and the spatial distribution of spectral emission coefficients was obtained from $L_{plasma}(\lambda)$ in the wavelength of 350.0–972.8 nm by spectral tomography calculation.

IV. DIAGNOSIS

A. Calculation of reduced population density distribution

This section describes the method for determining the spatial distribution of the number density of excited levels from the spatial distribution of the spectral radiance. Table I shows the optical emission lines employed in this study.

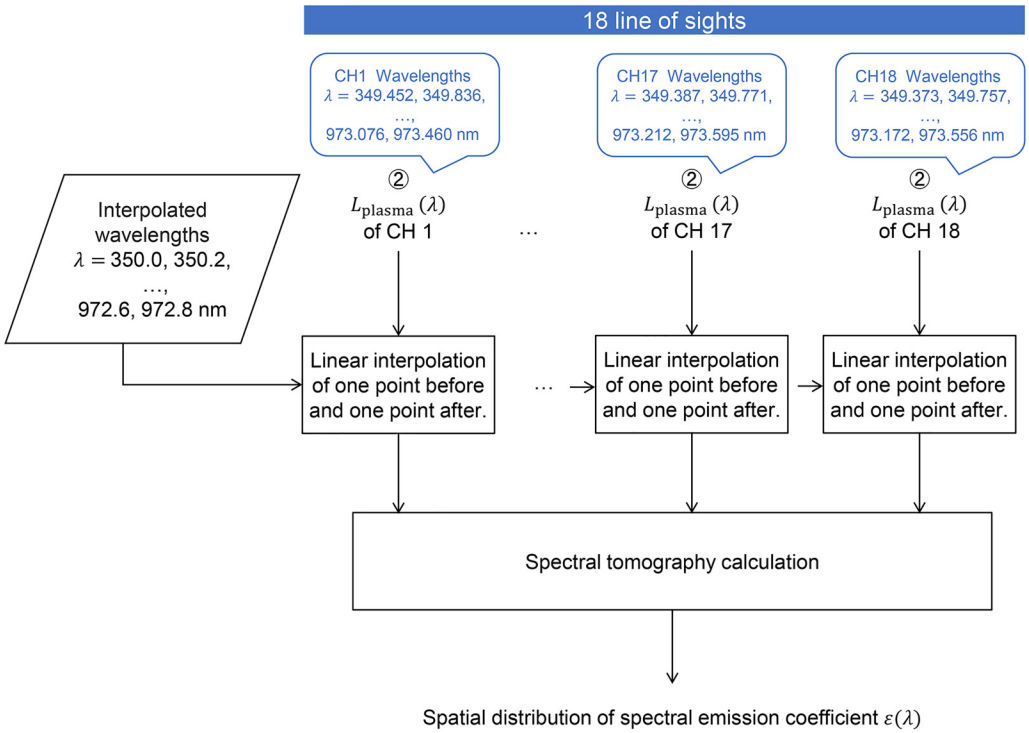

FIG. 6. Calculation flowchart of the spectral tomography.

The relationship between the spectral emission coefficient and the number density of the excited levels is expressed as follows:

$$4\pi \int_{-\infty}^{\infty} \varepsilon_{j^*\to i^*}(\lambda)\,\mathrm{d}\lambda = h\,\frac{c}{\lambda(j^*, i^*)}\,A(j^*, i^*)\,n_{j^*}, \tag{18}$$

where $\varepsilon_{j^*\to i^*}$ is the spectral emission coefficient of the transition from level j^* to level i^*, that is, the line spectral profile of the transition from level j^* to level i^*; h is the Planck constant, c is the speed of light, $\lambda(j^*, i^*)$ is the wavelength of the transition from level j^* to level i^*, $A(j^*, i^*)$ is Einstein's A coefficient of the transition from level j^* to level i^*, and n_{j^*} is the number density of level j^*.

When observing the line spectra nearby using a spectrometer with a large wavelength resolution, the hems of the line spectra overlap. Therefore, if the experimental data for spectral emission coefficients are integrated over the wavelength range, the emission coefficients for a given emission line cannot be determined correctly. To solve this problem, we separated adjacent line spectra by fitting the calculated value obtained using the Voigt function to the experimental data of the spectral emission coefficients. Then, the emission coefficients were obtained by integrating the line spectrum profiles (spectral emission coefficients) obtained using the Voigt function in the wavelength direction for each transition alone.

Prior studies with Abel transformations used the same transitions for all positions to diagnose. On the other hand in this study, in each pixel, emission lines were mechanically extracted from the experimentally obtained spectral emission coefficient data, and the extracted emission lines were used to obtain the excited-level number density distribution. Because the wavelength distribution and strength of the spectral emission coefficients differ greatly depending on the spatial location, there were no transitions that appeared in common for all pixels.

B. Argon CR model and diagnostics with the model

The Ar CR model[22] is an excitation kinetic model that provides a reduced population density distribution n_i/g_i with T_e, electron energy distribution function (EEDF), N_e, atomic temperature T_a, ion density N_I, and plasma radius r as input parameters. The rate equation is as follows:

$$\begin{aligned}\frac{\mathrm{d}n_i}{\mathrm{d}t} = &\sum_{j=i+1}^{65}\Big[-\{C(i,j)N_e n_i + K(i,j)n_1 n_i\} \\ &+\{F(j,i)N_e n_j + L(j,i)n_1 n_j + A(j,i)\Lambda_{j,i} n_j\}\Big] \\ &+\sum_{j=1}^{i-1}\Big[\{C(j,i)N_e n_j + K(j,i)n_1 n_j\} \\ &-\{F(i,j)N_e n_j + L(i,j)n_1 n_i + A(i,j)\Lambda_{i,j} n_i\}\Big] \\ &-\{S(i)N_e n_i + V(i)n_1 n_i\} \\ &+\big[\{O(i)N_e + W(i)n_1 + R(i)\Lambda_i\}\big]N_e N_I \\ &-\big[D(i) + B(i)\big] \quad (i = 2, 3, \ldots),\end{aligned} \tag{19}$$

TABLE I. Optical emission lines for OES measurement.

Ritz wavelength[21] in air $\lambda(j^*, i^*)$ [nm]	Upper level				Lower level				A coefficient[21]
	Vlček[22]		Racah[21]		Vlček[22]		Racah[21]		
	Level j	g_j	Level j^*	g_{j^*}	Level i	g_i	Level i^*	g_{i^*}	A (j^*, i^*) [s^{-1}]
708.6705	21	24	$6s'[1/2]^\circ_1$	3	10	1	$4p[1/2]_0$	1	1.50×10^5
794.8176	8	8	$4p'[3/2]_1$	3	4	1	$4s'[1/2]^\circ_0$	1	1.86×10^7
826.4521	9	3	$4p'[1/2]_1$	3	5	3	$4s'[1/2]^\circ_1$	3	1.53×10^7
840.8209	8	8	$4p'[3/2]_2$	5	5	3	$4s'[1/2]^\circ_1$	3	2.23×10^7
842.4647	7	20	$4p[5/2]_2$	5	3	3	$4s[3/2]^\circ_1$	3	2.15×10^7
852.1441	8	8	$4p'[3/2]_1$	3	5	3	$4s'[1/2]^\circ_1$	3	1.39×10^7
866.7943	7	20	$4p[3/2]_1$	3	4	1	$4s'[1/2]^\circ_0$	1	2.43×10^6
912.2967	6	3	$4p[1/2]_1$	3	2	5	$4s[3/2]^\circ_2$	5	1.89×10^7
922.4498	7	20	$4p[3/2]_2$	5	5	3	$4s'[1/2]^\circ_1$	3	5.00×10^6
935.4218	7	20	$4p[3/2]_1$	3	5	3	$4s'[1/2]^\circ_1$	3	1.06×10^6
965.7786	6	3	$4p[1/2]_1$	3	3	3	$4s[3/2]^\circ_1$	3	5.40×10^6

where C and F are the electron-collisional excitation and de-excitation rate coefficients, respectively; K and L are the atomic-collisional excitation and de-excitation rate coefficients, respectively; A is the radiative transition probability; S and O are the atomic-collisional ionization and electron three-body recombination rate coefficients, respectively; V and W are the atomic-collisional ionization and atomic three-body recombination rate coefficients, respectively; R is the radiative recombination rate coefficient; B is the rate of generation of metastable Ar_2 molecules, D is the diffusion loss of the metastable Ar atom; $\Lambda_{i,j}$ and Λ_i are the optical escape factors of the transition from level i to level j and the transition from ion level to level i, respectively. The rate coefficients were calculated based on reaction cross sections, which were function of T_e, N_e, p, r, T_a, or N_I, as shown in the study by Vlcek.[22] The quasistationary approximation ($d/dt = 0$) in Eq. (19) yields a set of simultaneous equations with T_e and N_e as input variables and n_i as the output variable. $\Lambda_{i,j}$ and Λ_i were calculated as shown in the study by Vlcek.[22] Optical thickness for transitions to the ground level $\Lambda_{i,1}$ was considered and to non-ground levels were assumed to be optically thin [$\Lambda_{i,j} = 1$ (for $j \neq 1$)].

In this study, T_e and N_e were determined by fitting the n_i/g_i distributions of the experimental values by OES measurements and the values calculated from the Ar CR model. The objective function f_I for the fitting[17,23,24] was assumed as follows:

$$f_I(T_e, N_e) = \sum_{i \in I} \left(\frac{n_{i\text{model}}(T_e, N_e)/g_i}{n_{i\text{OES}}/g_i} - 1 \right)^2, \tag{20}$$

where $n_{i\text{model}}(T_e, N_e)/g_i$ is the value of n_i/g_i from the Ar CR model and $n_{i\text{OES}}/g_i$ is the experimental value obtained from OES measurements; I is a set of optical emission lines that are employed for the fitting. In this study, 9, 10, or 11 optical emission lines shown in Table I for diagnosis were employed. T_e and N_e were obtained by fitting the minimization f_I.

V. RESULTS AND DISCUSSION

A. Spectral tomography

Figures 7–14 show the dependence of the spectral emission coefficient on the spatial position, pressure, and power. The spectral emission coefficient increased with increasing pressure and power. The spectral emission coefficient was generally higher in the center and lower in the periphery in the y-direction. For the z-direction, it was higher on the upper side, just below the antenna and window, and decreased downstream. The spatial distribution of spectral emission coefficient was different for each wavelength even at the same pressure and power. It denotes that each excited level had a different dependence on the spatial distribution.

In the central region where the lines-of-sight intersect, the spatial distribution could be observed at a high resolution; however, the resolution of the reconstructed images was inferior in the peripheral areas where the lines-of-sight did not intersect. In the peripheral area, there were areas that the spectral emission coefficients as a reconstructed value were negative values. In this experiment, the line-of-sight placement was concentrated in the center of the chamber, and thus, the spatial distribution of spectral emission coefficients at the periphery could not be adequately obtained. Therefore, uncertainty in image reconstruction may have been greater at the same area. In this study, subsequent analyses for diagnostics of T_e and N_e are discussed focusing only on the central region ($-10 \leq y\,[\text{cm}] \leq 10,\ -4 \leq z\,[\text{cm}] \leq 4$).

B. Diagnosis of electron temperature and density

Figure 15 shows the T_e diagnostic result as a dependence on pressure and spatial position. T_e decreased with increasing pressure. A possible mechanism behind this observation is that the increase in pressure increased the electron–atom collision frequency and reduced the high-energy component of the electrons.

Figure 16 shows the T_e diagnostic result as a dependence on power and spatial position. T_e increased monotonically with

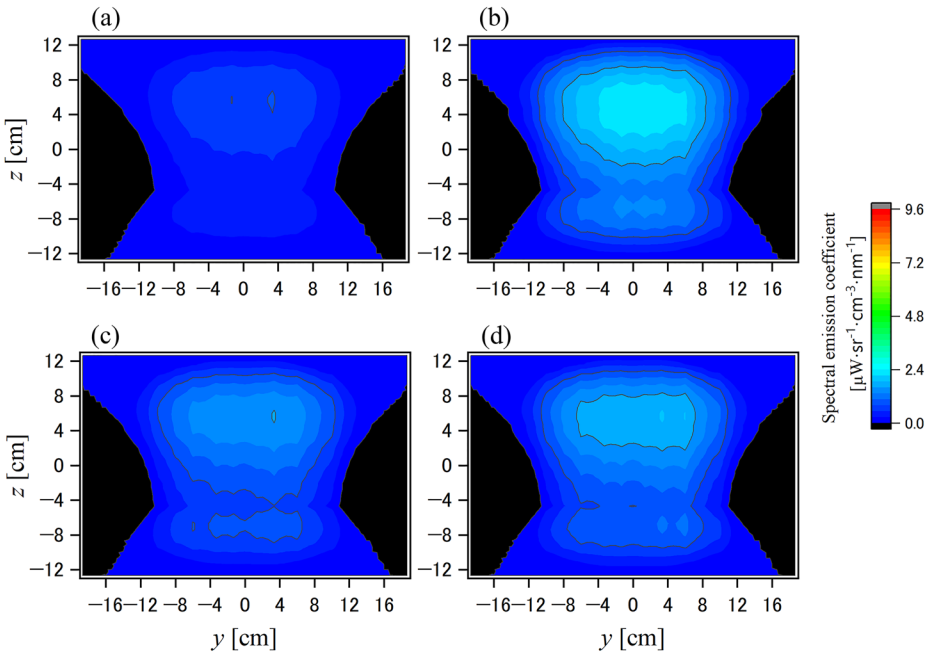

FIG. 7. Dependence of 708.6 nm of the spectral emission coefficient on the position and power at $p = 1$ Pa. (a), (b), (c), and (d) are the results at $P = 200$, 400, 600, and 800 W, respectively.

power from 200 to 400 W. It decreased once, from 400 to 600 W, and increased again from 600 to 800 W. The mechanism for the roughly monotonic increase in power and T_e is thought to be the increase in electromagnetic field strength that accompanied by the increase in power, which contributed to the acceleration of electrons. The cause of the decrease in T_e once at 400 to 600 W may have been a transition from the E-mode (capacitive discharge mode) to the H-mode (inductive discharge mode). The phenomenon that the T_e drops once at the transition from the E-mode to the H-mode even with increasing power is reported in a simulation of an argon ICP plasma at 6.7 Pa by Zhao *et al.*[25]

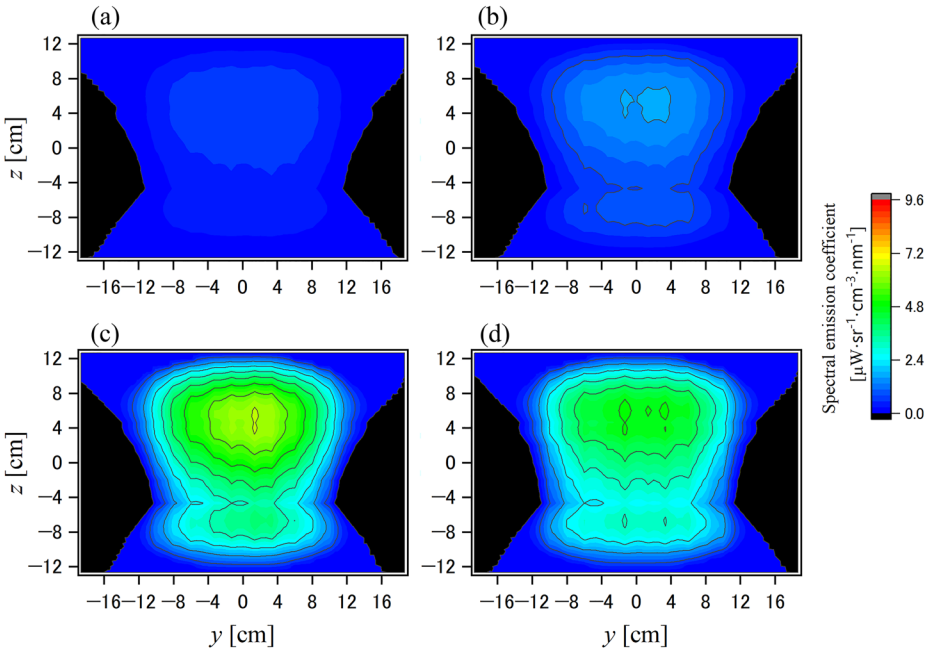

FIG. 8. Dependence of 708.6 nm of the spectral emission coefficient on the position and pressure at $P = 300$ W. (a), (b), (c), and (d) are the results at $p = 0.5$, 1, 5, and 10 Pa, respectively.

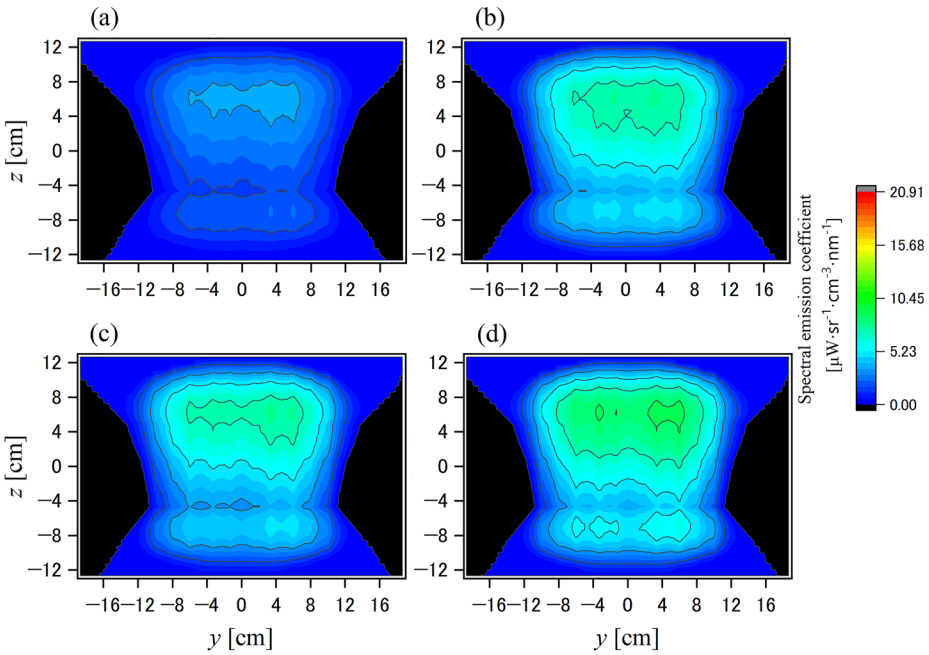

FIG. 9. Dependence of 750.4 nm of the spectral emission coefficient on the position and power at $p = 1$ Pa. (a), (b), (c), and (d) are the results at $P = 200$, 400, 600, and 800 W, respectively.

The y-direction dependence on T_e shows asymmetry higher in the center and lower in the periphery. The z-direction dependence on T_e shows higher in the upper side and lower in the lower side. This is because of the grounded window flange and the nonuniform-induced electromagnetic field distribution on the y–x plane and the asymmetry of the geometrical structure of the device, particularly the spiral antenna ends.[17]

Figure 17 shows the N_e diagnostic result as the dependence on pressure and spatial position. N_e decreased with increasing pressure. This may be due to the increase in ionization/desorption reactions caused by the increase in electron–atom collision frequency due to increased pressure. Figure 18 shows the N_e diagnostic result as a dependence on power and spatial position. N_e was generally constant regardless of the electric power. N_e exhibited a gradual

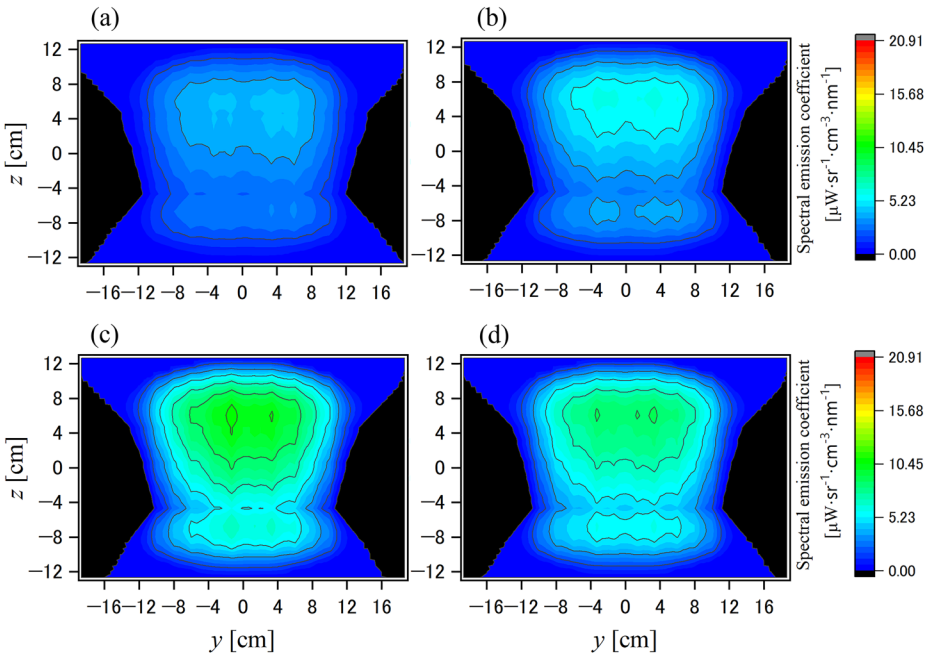

FIG. 10. Dependence of 750.4 nm of the spectral emission coefficient on the position and pressure at $P = 300$ W. (a), (b), (c), and (d) are the results at $p = 0.5$, 1, 5, and 10 Pa, respectively.

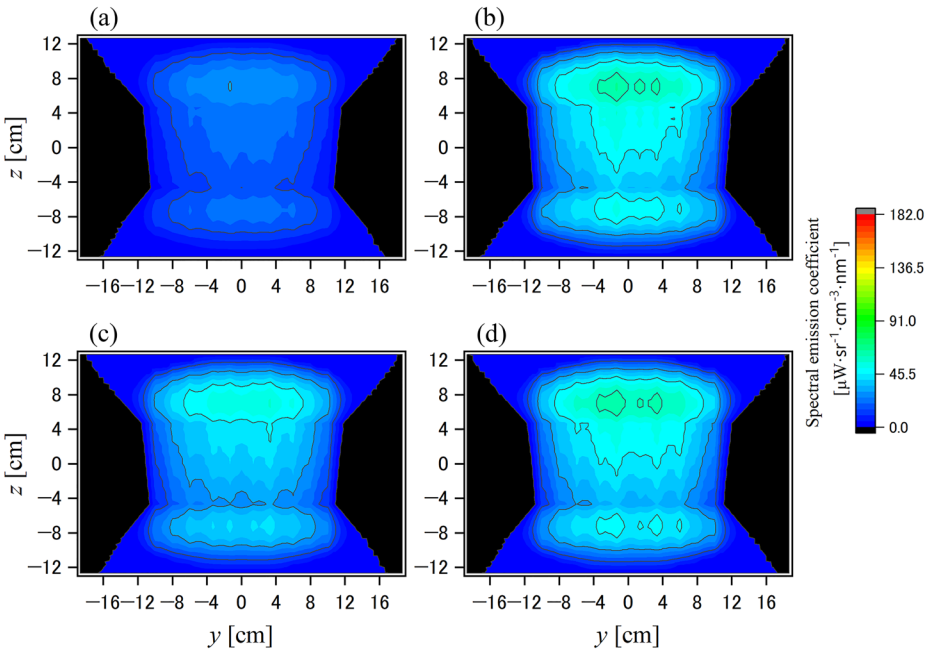

FIG. 11. Dependence of 811.8 nm of the spectral emission coefficient on the position and power at $p = 1$ Pa. (a), (b), (c), and (d) are the results at $P = 200$, 400, 600, and 800 W, respectively.

change in the spatial distribution, regardless of the geometric structure of the device. This is attributed to the significant influence of the diffusion effect on the wall and other factors. In addition, the spatial distribution was asymmetrical.

There is a previous literature[17] reporting electromagnetic field simulations for the experimental apparatus used in this study. In that simulation, the electromagnetic field distribution was asymmetric. The asymmetry of the electromagnetic field distribution was considered to be caused by the axially asymmetric shape of the spiral antenna. Note that in this study spontaneous emission transitions between excited levels were assumed to be optically thin. This assumption may be a cause of increased uncertainty of the diagnosis result of T_e and N_e in high-density plasmas.

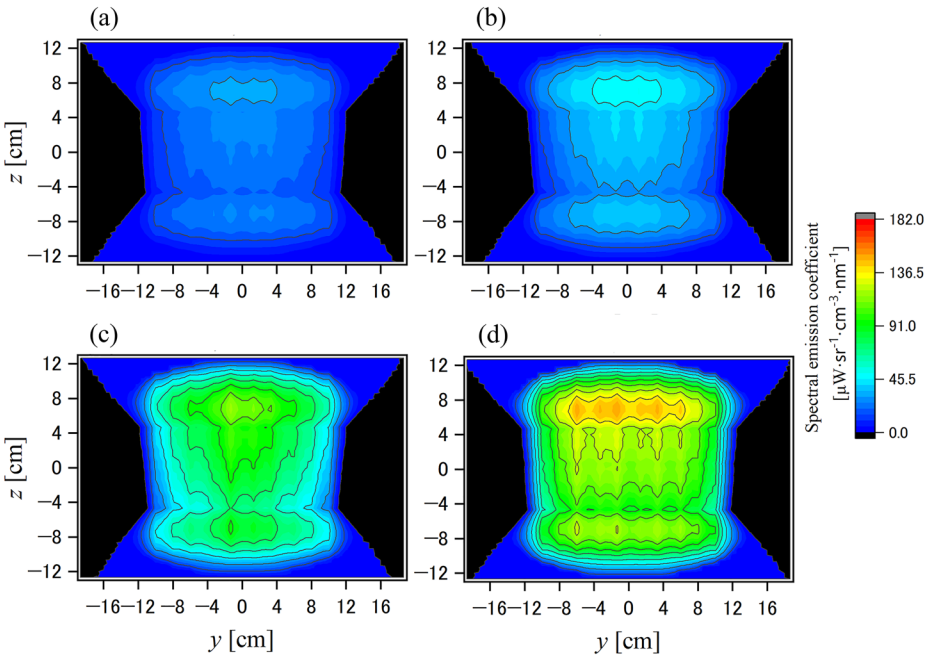

FIG. 12. Dependence of 811.8 nm of the spectral emission coefficient on the position and pressure at $P = 300$ W. (a), (b), (c), and (d) are the results at $p = 0.5$, 1, 5, and 10 Pa, respectively.

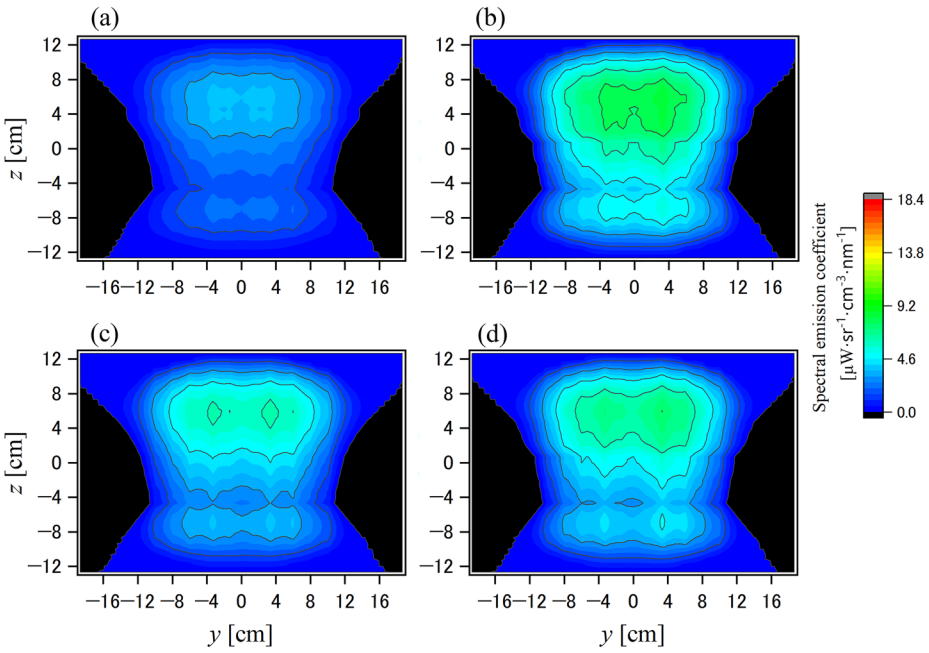

FIG. 13. Dependence of 965.8 nm of the spectral emission coefficient on the position and power at $p = 1$ Pa. (a), (b), (c), and (d) are the results at $P = 200$, 400, 600, and 800 W, respectively.

C. Discussion of uncertainty of spectral tomography and diagnosis

At the beginning, middle, and end in a series of experimental sequences with varying pressure and power, the spectral radiance was also measured at $p = 10$ Pa, $P = 800$ W three times in total. Figure 19 shows the average and range of the emission coefficient as the result of spectral tomography calculation at 708.6 nm on the three times measurements. T_e and N_e were diagnosed from the three times measurements independently, and their average and range were also obtained as shown in Figs. 20 and 21, respectively.

The range of the emission coefficient was largest in the area around $y = 0$ cm, $z = 8$ cm. It corresponds to the area near the quartz window just below the antenna, and it is possible that the repeated uncertainty in the impedance matching may have affected

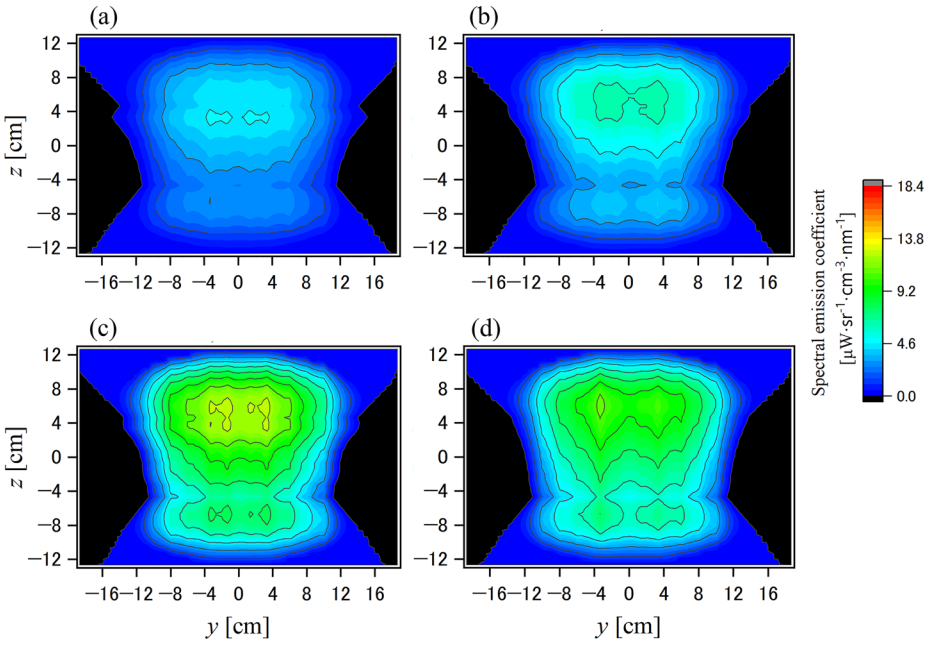

FIG. 14. Dependence of 965.8 nm of the spectral emission coefficient on the position and pressure at $P = 300$ W. (a), (b), (c), and (d) are the results at $p = 0.5$, 1, 5, and 10 Pa, respectively.

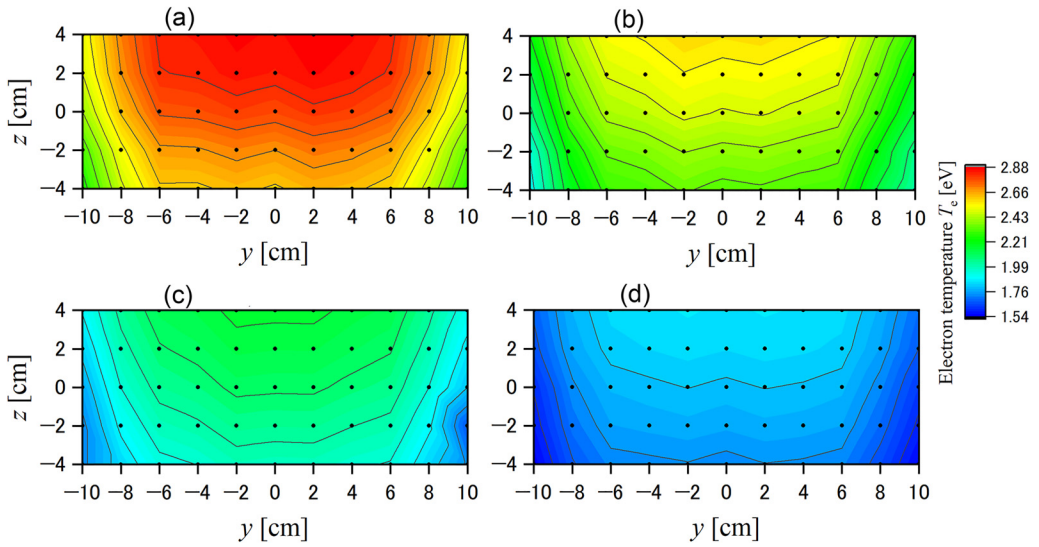

FIG. 15. Dependence of electron temperature on spatial position and pressure at $P = 300$ W. (a), (b), (c), and (d) are the results at $p = 0.5$, 1, 5, and 10 Pa, respectively.

the changed electromagnetic field generated by the antenna. In each of the three measurements, the variable capacitor constant of the auto-matcher changed in each trial. This suggests that the impedance of the plasma as the object of observation as well as the spectral emission coefficient distribution of the plasma itself changed from trial to trial. Hence, the range of spectral emission in the area located just below the antenna would have been larger. This result suggests that the uncertainty in plasma diagnostics performed by combining tomographic optical emission spectroscopy measurements and CR modeling will increase if all lines-of-sight are not acquired simultaneously. In particular, the simultaneous acquisition of all lines-of-sight is important for plasma diagnostics that combine tomographic optical emission spectroscopy and CR modeling.

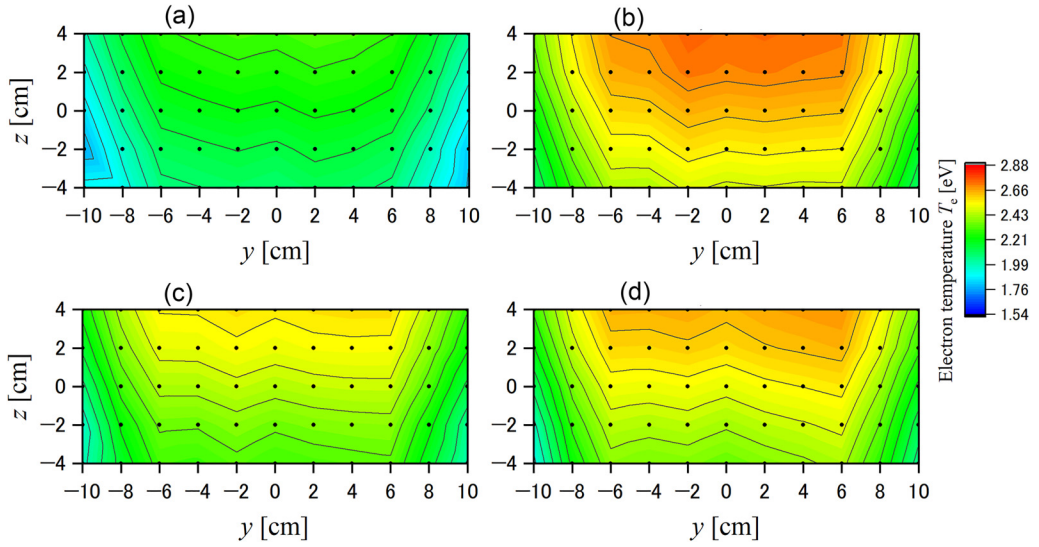

FIG. 16. Dependence of electron temperature on spatial position and RF power at $p = 1$ Pa. (a), (b), (c), and (d) are the results at $P = 200$, 400, 600, and 800 W, respectively.

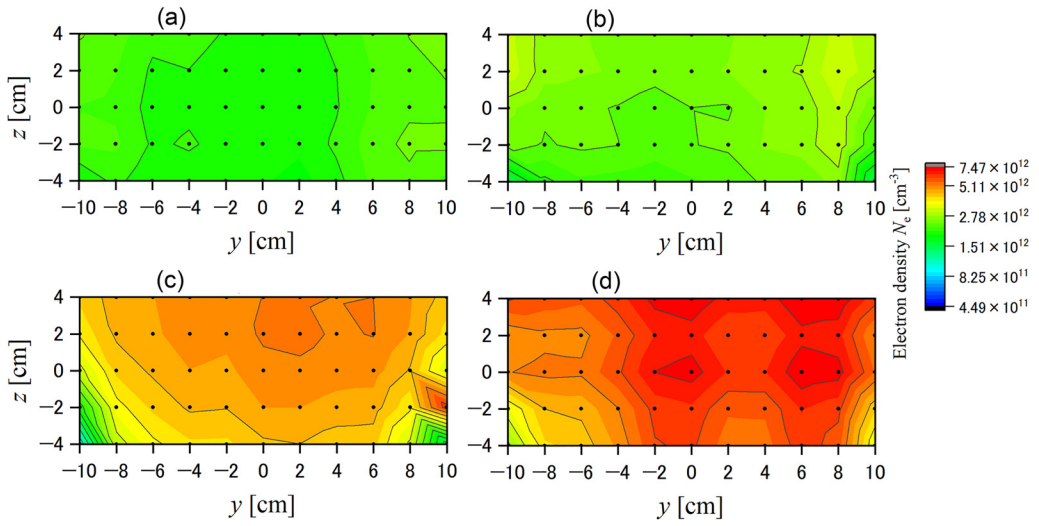

FIG. 17. Dependence of electron density on spatial position and pressure at $P = 300$ W. (a), (b), (c), and (d) are the results at $p = 0.5$, 1, 5, and 10 Pa, respectively.

This result suggests that in order to reduce the uncertainty of the spectral emission coefficient as a reconstructed image in tomographic optical emission spectroscopy, it is necessary to simultaneously acquire the spectral radiance of the entire line-of-sight of the cross section under observation. The position of the T_e maximum is just below the antenna, near $y = 0$ cm and $z = 4$ cm, the same position where the spectral emission coefficient reached its maximum value.

In other words, time evolution of the T_e of the plasma could be observed. The results further support the importance of the simultaneous acquisition of all lines-of-sight in plasma diagnostics based upon tomographic optical emission spectroscopy combined with the CR modeling, as mentioned above.

The areas around $y = 12$ to 16 cm, $z = -6$ to 4 cm and $y = -16$ to -12 cm, $z = -6$ to 4 cm also showed characteristic distributions. They correspond to the positions where the spectral emission coefficient as a reconstructed image exhibits a negative value and where there is no line-of-sight intersection. Furthermore, spectral emission coefficients in those areas are smaller than in other areas. Therefore, in those areas, it was considered that the

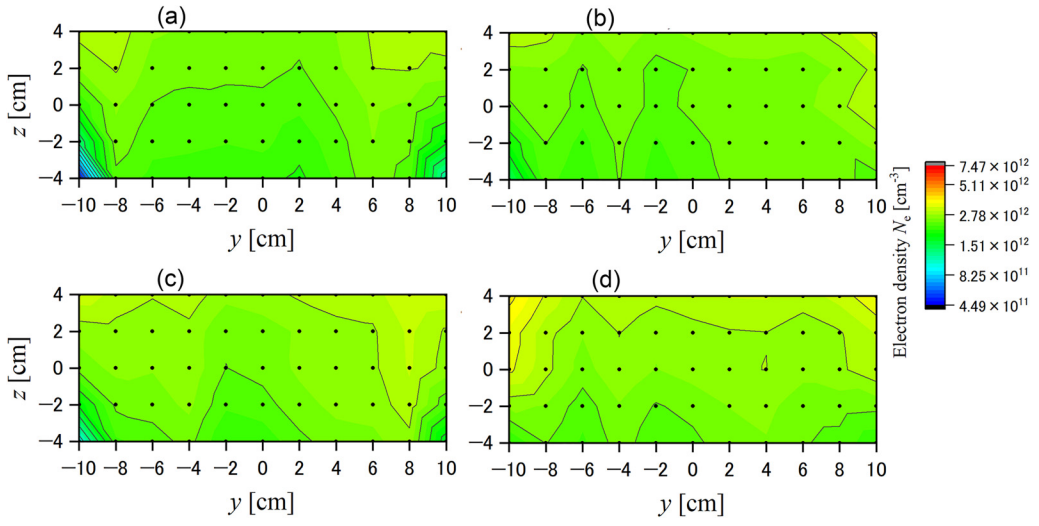

FIG. 18. Dependence of electron density on spatial position and power at $p = 1$ Pa. (a), (b), (c), and (d) are the results at $P = 200$, 400, 600, and 800 W, respectively.

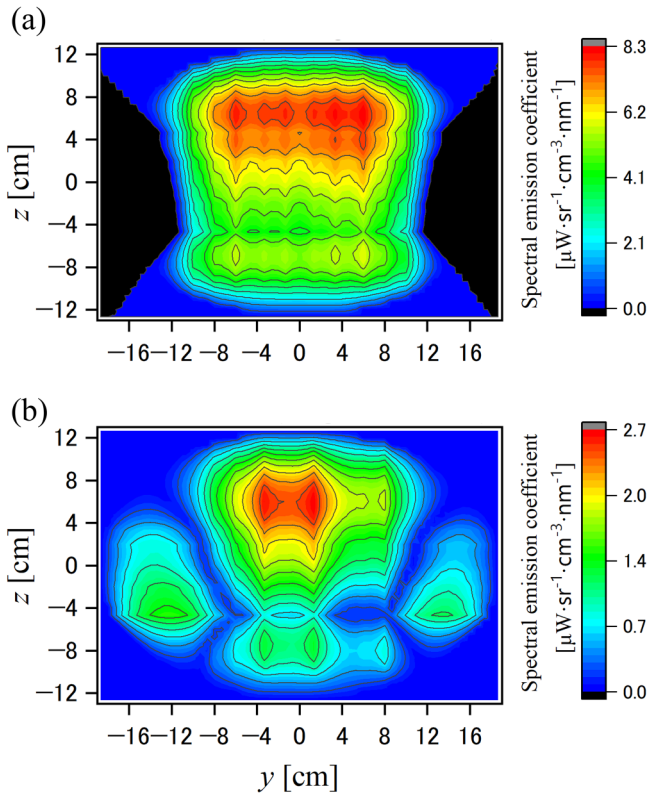

FIG. 19. Spacial dependence of spectral emission coefficient at 708.6 nm on $p = 10$ Pa, $P = 800$ W. (a) and (b) show the average and range of three times measurement, respectively.

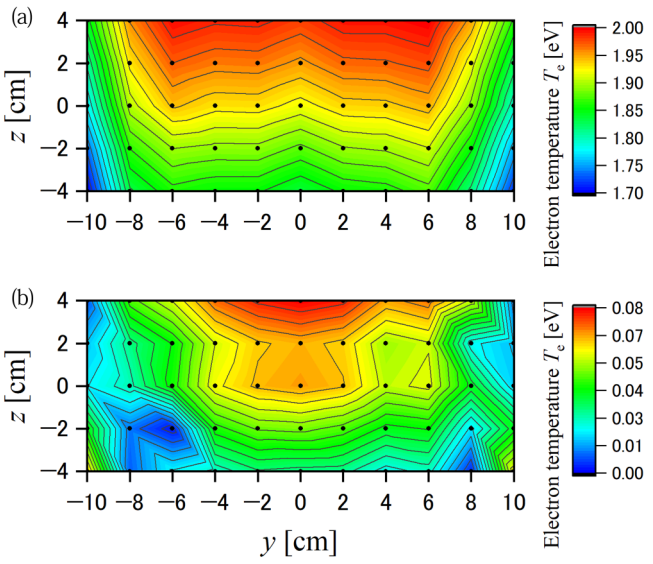

FIG. 20. Spacial dependence of electron temperature on $p = 10$ Pa, $P = 800$ W. (a) and (b) show the average and range of three times measurement, respectively.

signal-to-noise ratio on OES measurements was smaller. Therefore, the iterative uncertainty is considered to have increased.

The method was employed by this study, which simultaneously measures all the lines-of-sight of the measured cross section. As mentioned above, the method has the advantage that there is no uncertainty in the reconstructed image due to the time evolution of the plasma. However, in the same method, the number of lines-of-sight is generally lower than that of the line-of-sight scanning method due to objective overlap of lenses and equipment cost. In particular, the system in which plasma is observed from outside the observation window, as in this study, has the advantage of not disturbing the plasma in the depressurization process. However, the method has the disadvantage of the limitation of the number or placement of lines-of-sight. Future work is to improve the spectral tomography algorithm.

On the other hand, the range of N_e was spatially nearly uniform. This is thought to be because the absolute value of N_e was nearly uniform spatially, and the effect on repeatability was small.

To discuss the fitting uncertainty of Eq. (20), the reduced population density: n_{imodel}/g_i was recursively calculated by Ar CR model to substitute T_e and N_e, which were diagnosed by the fitting of the Ar CR model as shown in Figs. 20 and 21. Figure 22 shows the result. The difference between n_{iOES}/g_i and n_{imodel}/g_i was larger in Vlcek level number $i = 21$ compared to $i = 6$, 7, 8, and 9. It is due to the absolute value of the spectral radiance of the transition that was small, so the uncertainty of n_{iOES} becomes large.

Figure 23 shows the dependence of the optical escape factor from ion level on excitation state levels. The levels except for the

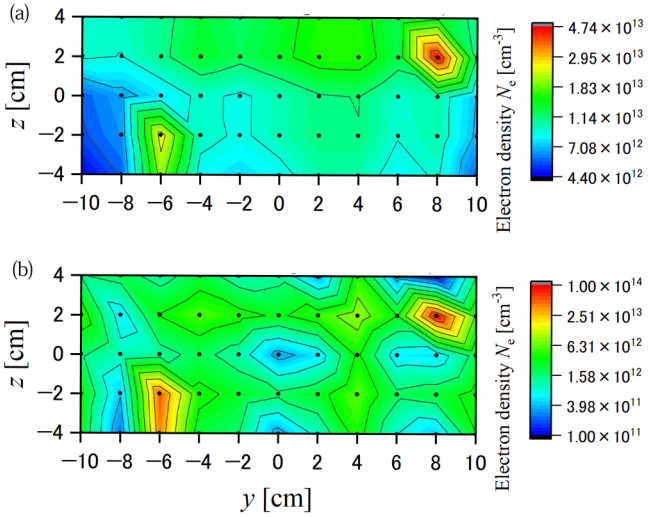

FIG. 21. Spacial dependence of electron density on $p = 10$ Pa, $P = 800$ W. (a) and (b) show the average and range of three times measurement, respectively.

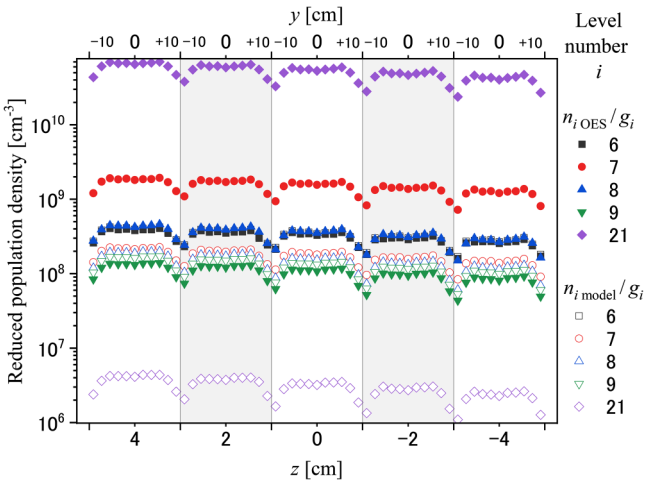

FIG. 22. Dependence of reduced population density of electron density on the position at $p = 10$ Pa, $P = 800$ W. This figure shows the result of the average of three times measurements.

Vlcek level numbers 3, 5, 12, 15, 16, 17, 20, 21, 26, 27, and 33 were optically thin, i.e., their optical escape factors were equal to one. Vlcek level 21 was the only nonone in the levels that were employed for fitting in this study as shown in Table I. This may have affected the convergence of same-level fitting. In this study, the results are presented using the CR model that considers optical thickness for some transitions, as shown in Eq. (19).

To discuss optical escape factor, we attempted to fit T_e and N_e under assuming optically thin for all transitions, but the results did not converge within the search range. This result suggests the validity of the model employed in this study. However, the model does not take into account the optical thickness between the excited levels, which is an issue for future work.

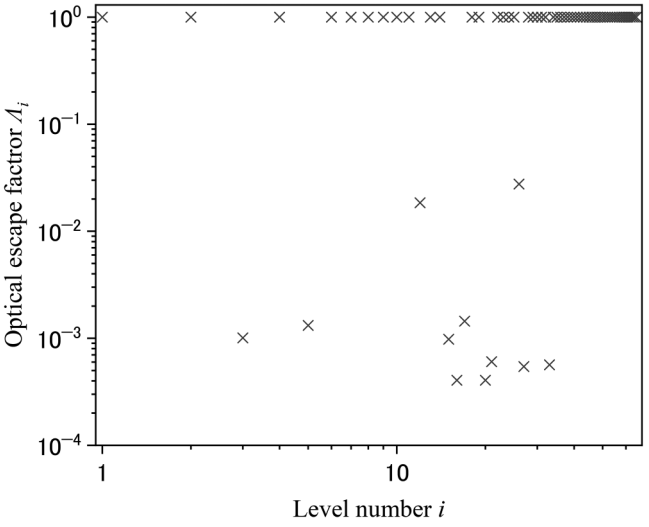

FIG. 23. Optical escape factor $p = 10$ Pa, $P = 800$ W. This figure shows the results of the average of three measurements, with data points in the range -10 cm $\leq y \leq 10$ cm and -4 cm $\leq z \leq 4$ cm on Figs. 20 and 21.

VI. CONCLUSION

An optical system was constructed to simultaneously acquire the spectral radiance of 18 lines-of-sight for tomographic OES measurement of low-pressure inductively coupled plasma. The optical system is located outside of the plasma system, which means that it is an undisturbing plasma diagnostic technique and highly applicable to process equipment. The position dependence of the spectral emission coefficients was obtained from the spectral radiance by spectral tomography calculations. The spatial distribution of the number density of excited levels was obtained based on the emission line spectra. The spatial distribution of the excited level number density was analyzed based on a CR model to diagnose the spatial distribution of T_e and N_e.

The effects of antenna power and total pressure on T_e and N_e are revealed. The effect of the placement of line-of-sight and plasma time evolution on T_e and N_e from spectral tomography measurements and CR modeling is discussed.

ACKNOWLEDGMENTS

The authors are grateful to Akira Kobayashi, Sotaro Hosoya, and Kazuma Yoneda of Tokyo Institute of Technology (then) for the helpful discussions and the assistance with the experiment and analysis. The authors are grateful to Masaki Yokoi and Yoko Sato of HORIBA STEC, Co., Ltd. and Kengo Yasui, Takumi Miyaoka, and Masayuki Sakurai of HORIBA, Ltd. for lending the multichannel spectrometer and advising on measurements using the spectrometer. This work was supported by JST SPRING Grant No. JPMJSP2106 and JSPS KAKENHI Grant No. JP23KJ0884.

AUTHOR DECLARATIONS

Conflict of Interest

The authors have no conflicts to disclose.

Author Contributions

Yuya Yamashita: Conceptualization (equal); Data curation (lead); Formal analysis (lead); Investigation (lead); Methodology (equal); Software (lead); Visualization (lead); Writing – original draft (lead); Writing – review & editing (lead). **Kenta Doi:** Conceptualization (equal); Investigation (supporting); Methodology (equal); Resources (equal); Visualization (supporting); Writing – review & editing (equal). **Tetsuji Kiyota:** Conceptualization (equal); Investigation (supporting); Project administration (lead); Resources (equal); Writing – review & editing (equal). **Kenta Ishi:** Investigation (equal); Writing – review & editing (equal). **Shuhei Watanabe:** Investigation (equal); Writing – review & editing (equal). **Wataru Kikuchi:** Software (equal); Writing – review & editing (equal). **Atsushi Nezu:** Investigation (supporting); Resources (supporting). **Hiroshi Akatsuka:** Conceptualization (equal); Supervision (lead); Writing – review & editing (equal).

DATA AVAILABILITY

The data that support the findings of this study are available from the corresponding author upon reasonable request.

REFERENCES

[1]R. Decoste, Rev. Sci. Instrum. **56**, 806 (1985).
[2]R. S. Granetz and P. Smeulders, Nucl. Fusion **28**, 457 (1988).
[3]T. Hermann, S. Löhle, S. Fasoulas, and A. Andrianatos, Appl. Opt. **55**, 10290 (2016).
[4]R. Barni, P. Alex, E. Ghorbanpour, and C. Riccardi, Eur. Phys. J. D **75**, 101 (2021).
[5]Y. Miyoshi, Z. L. Petrovic, and T. Makabe, J. Phys. D: Appl. Phys. **35**, 454 (2002).
[6]Y. Miyoshi, Z. L. Petrovic, and T. Makabe, IEEE Trans. Plasma Sci. **30**, 130 (2002).
[7]M. A. Lieberman and A. J. Lichtenberg, *Principles of Plasma Discharges and Materials Processing*, 2nd ed. (John Wiley & Sons Inc., Hoboken, NJ, 2005).
[8]X. Wan, S. L. Yu, G. Y. Cai, Y. Q. Gao, and J. L. Yi, J. Opt. Soc. Am. A **21**, 1161 (2004).
[9]K. Rathore, S. Bhattacharjee, D. N. Patel, and P. Munshi, IEEE Trans. Plasma Sci. **45**, 2492 (2017).
[10]V. Gonzalez-Fernandez, P. David, R. Baude, A. Escarguel, and Y. Camenen, Sci. Rep. **10**, 5389 (2020).
[11]T. Fujimoto, *Plasma Spectroscopy* (Oxford University, Oxford, 2004).
[12]D. Lee, J. Kim, G. Doh, C. Shin, and W. Choe, Plasma Sources Sci. Technol. **31**, 125004 (2022).
[13]S. Park, W. Choe, S. Y. Moon, and S. J. Yoo, Adv. Phys.: X **4**, 1526114 (2019).
[14]J. Jang, S. Park, J. Y. Park, and W. Choe, Plasma Sources Sci. Technol. **27**, 10LT01 (2018).
[15]*Shinpan Hikari-no-keisoku-manyuaru*, edited by Shoumei-gakkai [Nihon-riko-shuppankai (succeed by Japan Industrial Publishing), Tokyo, 2022] (in Japanese).
[16]"Methods of color measurement—Light-source color," Japanese Industrial Standards **JIS Z 8274:2015** (2015).
[17]Y. Yamashita, K. Doi, T. Kiyota, K. Asakawa, S. Hosoya, W. Kikuchi, A. Nezu, and H. Akatsuka, Rev. Sci. Instrum. **94**, 083503 (2023).
[18]M. Anton, H. Weisen, M. J. Dutch, W. v. d. Linden, F. Buhlmann, R. Chavan, B. Marletaz, P. Marmillod, and P. Paris, Plasma Phys. Control. Fusion **38**, 1849 (1996).
[19]D. R. Ferreira, seehttps://github.com/diogoff/isttok-tomography for "isttok-tomography" [Online] (2019).
[20]P. J. d. P. Carvalho, "Tomography algorithms for real-time control in ISTTOK," Ph.D. thesis (Instituto Superior Técnico, 2010).
[21]A. Kramida, Yu. Ralchenko, J. Reader, and NIST ASD Team, see https://physics.nist.gov/asd for "NIST Atomic Spectra Database" [Online]. National Institute of Standards and Technology, Gaithersburg, MD (2022).
[22]J. Vlcek, J. Phys. D: Appl. Phys. **22**, 623 (1989).
[23]Y. Yamashita, T. Akiba, T. Iwanaga, H. Yamaoka, S. Date, and H. Akatsuka, Jpn. J. Appl. Phys. **60**, 046003 (2021).
[24]Y. Yamashita, T. Akiba, T. Iwanaga, H. Yamaoka, S. Date, and H. Akatsuka, IEEE Trans. Plasma Sci. **50**, 1875 (2022).
[25]S.-X. Zhao, X. Xu, X.-C. Li, and Y.-N. Wang, J. Appl. Phys. **105**, 083306 (2009).